



## Superior photocatalytic properties of carbonized PANI/TiO<sub>2</sub> nanocomposites



Marija Radoičić<sup>a</sup>, Gordana Ćirić-Marjanović<sup>b</sup>, Vuk Spasojević<sup>a</sup>, Phil Ahrenkiel<sup>c</sup>, Miodrag Mitrić<sup>a</sup>, Tatjana Novaković<sup>d</sup>, Zoran Šaponjić<sup>a,\*</sup>

<sup>a</sup> "Vinča" Institute of Nuclear Sciences, University of Belgrade, P.O. Box 522, 11001 Belgrade, Serbia

<sup>b</sup> Faculty of Physical Chemistry, University of Belgrade, Studentski Trg 12-16, 11158 Belgrade, Serbia

<sup>c</sup> South Dakota School of Mines & Technology, Rapid City, SD 57701, USA

<sup>d</sup> IChTM –Department of Catalysis and Chemical Engineering, University of Belgrade, Njegoševa 12, 11000 Belgrade, Serbia

### ARTICLE INFO

#### Article history:

Received 10 March 2017

Received in revised form 4 May 2017

Accepted 6 May 2017

Available online 8 May 2017

#### Keywords:

Photocatalysis

TiO<sub>2</sub>

Carbonized polyaniline

### ABSTRACT

A simple bottom-up method for the preparation of novel and very efficient photocatalytic nanocomposite system based on carbonized form of polyaniline (PANI) and colloidal TiO<sub>2</sub> nanocrystals has been developed. The carbonized PANI/TiO<sub>2</sub> nanocomposites were synthesized in a two-step procedure. Firstly, non-carbonized PANI/TiO<sub>2</sub> nanocomposites were synthesized by the chemical oxidative polymerization of aniline (ANI) with ammonium peroxydisulfate, in the presence of colloidal TiO<sub>2</sub> nanoparticles (TiO<sub>2</sub> NPs) (d ~ 4.5 nm). Initial [TiO<sub>2</sub>]/[ANI] mole ratios were 20, 50, and 80. In the second step, following the polymerization process, the carbonization of PANI/TiO<sub>2</sub> nanocomposites was performed by thermal treatment in an inert atmosphere at 650 °C. The morphological and structural properties of the carbonized nanocomposites were studied using transmission electron microscopy (TEM), scanning electron microscopy (SEM), X-ray powder diffraction (XRD) and Raman spectroscopy. The accomplishment of complete carbonization of PANI in PANI/TiO<sub>2</sub> nanocomposites was confirmed by Raman spectroscopy. The appearance of anatase and rutile crystal forms in TiO<sub>2</sub> NPs upon carbonization, with mass ratio depending on the initial molar ratio of ANI and TiO<sub>2</sub> NPs was revealed by XRD measurements, TEM, SEM and Raman spectroscopy. The photocatalytic activities of carbonized PANI/TiO<sub>2</sub> nanocomposites were evaluated following the photocatalytic degradation processes of Rhodamine B and Methylene blue. Carbonized PANI/TiO<sub>2</sub> nanocomposites showed higher photocatalytic efficacy compared to bare TiO<sub>2</sub> NPs and non-carbonized PANI/TiO<sub>2</sub> nanocomposites. The porosity and surface structure of carbonized PANI/TiO<sub>2</sub> nanocomposites, as well as crystalline structure of TiO<sub>2</sub>, affect photocatalytic activity of nanocomposites.

© 2017 Elsevier B.V. All rights reserved.

### 1. Introduction

Nanoparticulate anatase titanium dioxide (TiO<sub>2</sub>) has proven as an efficient UV light-harvesting materials for photocatalytic removal of organic pollutants and to a lesser extent for photocatalytic water splitting [1]. The widespread use of TiO<sub>2</sub> nanocrystals of various crystalline structures and shapes in photoinduced processes is mainly based on its simple synthesis, low cost, and ability to resist photocorrosion. However, the fact that TiO<sub>2</sub> utilizes only ~5% of the solar light led to development of many new strate-

gies for tuning optical response of TiO<sub>2</sub> in visible region with aim to increase its photoactivity [2]. On the other hand, similar importance was given to the photoinduced charge mobility/separation, which must be also improved in anticipation of an increase of the overall photoefficiency of TiO<sub>2</sub> [2]. One of many reported approaches that can meet both demands, visible light absorption and non-hindered charge separation in TiO<sub>2</sub>, is the synthesis of nanocomposite systems based on electronically coupled conductive polymers (e.g., PANI, polythiophene, polypyrrole, and their derivatives) and TiO<sub>2</sub> [3–5]. Namely, moderate to high mobility of charge carriers in extended  $\pi$ -conjugated electron systems, such as conductive polymers which are electronically coupled to TiO<sub>2</sub>, allows for better separation of photoinduced charges in TiO<sub>2</sub> nanocrystals. In general, hybrid functional materials consisting of conductive polymers and various nanoparticles exhibit some unique properties that usually may not be observed in the individual components [6–13].

\* Corresponding author at: Laboratory for Radiation Chemistry and Physics, "Vinča" Institute of Nuclear Sciences, University of Belgrade, P.O. 522, 11001 Belgrade, Serbia.

E-mail address: [saponjic@vinca.rs](mailto:saponjic@vinca.rs) (Z. Šaponjić).

Recently, we reported the simple synthesis of photocatalytically active PANI/TiO<sub>2</sub> nanocomposite material, which was tested in photodegradation reactions of the model compounds Methylene blue and Rhodamine B, and showed higher photocatalytic efficacy compared to bare TiO<sub>2</sub> nanocrystals [14].

Besides the previously mentioned roles of N-containing conductive polymers (PANI or polypyrrole) in photoinduced charge-transfer processes, they can be also used to produce new N-containing 1-D nanostructured carbon materials by the carbonization process at high temperature (500–1050 °C) and in an inert atmosphere [14–22]. Nanocomposites of such N-containing carbonaceous materials and various inorganic components (metals, oxides) offer additional possibilities/improvements in various applications [23–25]. The development of carbon-nanostructure based titania nanocomposites opens the possibility to design the photocatalysts with tailored properties [26]. For example, N-doped graphene in the photocatalytic metal-oxide based nanocomposite materials serves as a charge acceptor, due to its two-dimensional  $\pi$ -conjugation structure [27,28]. Also, N-doping minimizes the defects in graphene structures, such as vacancies and disrupted in-plane conjugation sites, resulting in more effective charge transfer and consequently better charge separation in metal oxides [29]. Nanocomposites based on SnO<sub>2</sub> and ZnO coated nitrogen-containing carbon nanotubes showed increased photocatalytic activity toward model molecules, due to suppressed recombination of photogenerated charges in metal oxides, which is caused by effective transfer of conduction-band electrons to carbon nanotubes [30,31].

Conventional photoactive nanocomposites based on carbonaceous materials and TiO<sub>2</sub> nanocrystals usually were synthesized by demanding methods using expensive equipment or at high temperature. Generally, in these nanocomposites the nanostructure is not well defined which induces an unsatisfactory degree of dispersibility and additionally interaction of carbonaceous part and TiO<sub>2</sub> NPs is weak which prevents efficient functionalization of TiO<sub>2</sub> nanocrystals [32]. In this study, photocatalytic performances of carbonized PANI/TiO<sub>2</sub> nanocomposites along with their structural and morphological properties were, to the best of our knowledge, reported for the first time. Our approach significantly facilitates the synthesis of the very efficient photocatalytic nanocomposite materials based on carbon structures and TiO<sub>2</sub> nanocrystals. In order to explore the influence of carbonization of PANI on the photocatalytic efficiency of the nanocomposites and compare it with photoactivities of non-carbonized PANI/TiO<sub>2</sub> nanocomposites and bare TiO<sub>2</sub> nanocrystals, we have followed degradation processes of model molecules (Methylene blue and Rhodamine B). Structural (molecular and crystalline) properties were studied by Raman spectroscopy and X-ray powder diffraction (XRD) in order to test the influence of carbonization process and amount of PANI on crystalline structure of TiO<sub>2</sub> NPs which is of great importance for the overall photocatalytic activity of nanocomposites. The optical properties were studied by UV–vis reflectance spectroscopy while the morphological properties of synthesized carbonized PANI/TiO<sub>2</sub> nanocomposites were studied by transmission electron microscopy (TEM) and scanning electron microscopy (SEM). A significant improvement of photocatalytic activity of carbonized PANI/TiO<sub>2</sub> nanocomposites compared to non-carbonized nanocomposites studied in our previous work [14] was observed.

## 2. Experimental

### 2.1. Materials

All chemicals (Aldrich, Fluka) were reagent-grade and used as-received except aniline (ANI), (Centrohem, Serbia, p.a. > 99.5%)

**Table 1**

Amounts of reagents used for the syntheses of TP nanocomposites.

Sample Reagent content	TPC-20	TPC-50	TPC-80
0.2 M TiO <sub>2</sub> (ml)	80	80	80
Aniline ( $\mu$ L)	73.04	29.2	18.3
APS (g)	0.2282	0.0913	0.0571

which was distilled under reduced pressure and stored at room temperature, under Ar, prior to use. Ammonium peroxydisulfate (APS) (analytical grade, Centrohem, Serbia) was used as received. Milli-Q deionized water was used as a solvent.

### 2.2. Synthesis of colloidal TiO<sub>2</sub> NPs

The colloidal dispersion of TiO<sub>2</sub> NPs was prepared in a manner analogous to the procedure proposed by Rajh et al. [33]. The TiCl<sub>4</sub>, cooled to –20 °C, was added drop-wise to cooled water (at 4 °C) under vigorous stirring and then kept at this temperature for 30 min. The initial pH of the solution was between 0 and 1 depending on the TiCl<sub>4</sub> concentration. The slow growth of particles was attained by applying dialysis (three days) against water (changed daily) at 4 °C until the pH of the solution reached 3. The Spectra/Por Dialysis Membrane, MWCO: 3500 (Spectrum Laboratories, Inc., Rancho Dominguez, CA) was used for the dialysis of the colloidal dispersion. The concentration of TiO<sub>2</sub> dispersion was determined from the concentration of the peroxide complex obtained after dissolving the TiO<sub>2</sub> NPs in concentrated H<sub>2</sub>SO<sub>4</sub> [34].

### 2.3. Synthesis of carbonized PANI/TiO<sub>2</sub> nanocomposites

The carbonized PANI/TiO<sub>2</sub> nanocomposites were synthesized in a two-step procedure. The first step included the synthesis of PANI/TiO<sub>2</sub> nanocomposites by chemical oxidative polymerization of aniline by oxidant (APS) in the presence of colloidal TiO<sub>2</sub> NPs [14], at room temperature. The initial [TiO<sub>2</sub>]/[ANI] mole ratios of synthesized PANI/TiO<sub>2</sub> nanocomposites were 20, 50 and 80 and the samples are designated in further text as TP-20, TP-50 and TP-80, respectively. The initial [APS]/[ANI] mole ratio was 1.25. The aqueous solution of APS (0.025–0.1 M, 10 mL) and aniline (0.02–0.1 mM, 10 mL) was simultaneously poured into the colloidal TiO<sub>2</sub> solution (0.2 M, 80 mL). The amounts of reagents used for the synthesis of TP nanocomposites are included in Table 1. Due to the relatively low concentration of ANI, the reactions of polymerization were slow and, for that reason, the reaction mixtures were stirred for 3 days. In order to remove residual monomer, oxidant, and low-molecular weight fractions, which are formed during the polymerization process, the post-synthetic dialysis of TP nanocomposites against Milli-Q deionized water was applied. After dialysis, the nanocomposite samples were dried in a vacuum oven at 60 °C until a constant mass was reached. In the second step, the carbonization of powder samples of TP nanocomposites in an argon atmosphere was performed by ramping temperature up from room temperature to 650 °C, holding at this temperature for 15 min, and cooling to room temperature. The 30 min before and during the heating and cooling processes, the samples were saturated in an argon atmosphere. The obtained materials are code-named by their initial [TiO<sub>2</sub>]/[ANI] mole ratio as follows: TPC-20, TPC-50 and TPC-80, respectively.

### 2.4. Characterization

Raman spectra of all nanocomposite samples were recorded after excitation by a HeNe gas laser (at an excitation wavelength of 633 nm) and collected on a Thermo Scientific DXR Raman microscope, equipped with a research optical microscope and a CCD

detector. The laser beam was focused on the sample placed on an X-Y motorized sample stage using an objective magnification of 50 $\times$ . The scattered light was analyzed by the spectrograph with a 600 lines-per-mm grating. Laser power at the sample was 0.5 mW.

The X-ray powder diffraction patterns (XRD) of nanocomposite samples were obtained by a Philips PW 1050 powder diffractometer with Ni filtered Cu K $\alpha$  radiation ( $\lambda = 1.5418 \text{ \AA}$ ). The diffraction intensity was measured by the scanning technique (a step size of 0.05 $^\circ$  and a counting time of 50 s per step).

The TiO $_2$  NPs size and the thickness of carbonized PANI layer were determined by transmission electron microscopy (TEM). TEM images were obtained on a JEOL JEM-2100 LaB $_6$  TEM operated at 200 KeV.

Diffusion reflectance UV–vis spectra were recorded by UV-2600 Shimadzu spectrophotometer (Shimadzu Corporation, Tokyo, Japan) equipped with an integrated sphere (ISR-2600 Plus (for UV-2600)).

The LECO Elemental Analyzer CHNS-628 Model was used for the elemental analysis (N and C content) of carbonized PANI/TiO $_2$  nanocomposite samples.

Measurements of textural properties (specific surface area, pore size and pore volume) of nanocomposites were carried out using an automatic sorption apparatus (Sorpomatic 1990 Thermo Finnigen). The nitrogen adsorption was performed at  $-196^\circ\text{C}$ , with a relative pressure interval between 0.05 and 0.98. Before each measurement the sample was degassed at  $200^\circ\text{C}$  under vacuum for period of 4–10 h to avoid significant changes in vacuum stability. The adsorbed amount of nitrogen was measured by volume at standard temperature and pressure. The specific surface areas ( $S_{\text{BET}}$ ) were calculated by the BET method [35–37], from nitrogen adsorption–desorption isotherms, using data up to  $p/p_0 = 0.3$ . The pore size distribution has been computed from the desorption branch of the isotherms [37].

The elemental analysis of the surface of carbonized PANI/TiO $_2$  nanocomposites and mapping of Ti was carried out by a JEOL-6610LV scanning electron microscope, with EDS detector (model: X-Max Large Area Analytical Silicon Drift connected with INCA Energy 350 Microanalysis System).

The thermogravimetric analysis (TGA) was carried out using TGA701 Thermogravimetry Analyzer with oxygen purging gas, at a flow rate of  $20 \text{ mL min}^{-1}$  and at a heating rate of  $10^\circ\text{C min}^{-1}$ .

## 2.5. Photocatalytic activity measurements

The photocatalytic activities of synthesized samples were examined by following degradation processes of test dye molecules: Rhodamine B (RB) and Methylene blue (MB). The 50 mL of  $1 \times 10^{-5} \text{ mol L}^{-1}$  dye aqueous solutions (pH = 5.77 for MB, pH = 5.34 for RB) were mixed with  $1 \text{ g L}^{-1}$  of the TPC photocatalyst or bare colloidal TiO $_2$  nanoparticles. Prepared dispersions were continuously stirred and illuminated in air by a lamp that simulated solar irradiation (Osram Vitalux lamp, 300 W, white light: UVB (280–315 nm) radiated power was 3.0 W; UVA (315–400 nm) radiated power was 13.6 W; the rest were visible light and IR). Optical power was measured using an R-752 Universal Radiometer, read out with sensor (model PH-30 DIGIRAD) was found to be  $\sim 30 \text{ mW cm}^{-2}$  at a distance of 30 cm from experimental dispersion. Before illumination, dispersions were stirred 30 min in the dark, enabling adsorption-desorption equilibrium. At the beginning, dispersion sampling (1 mL) is carried out every 5 min during the first half hour of illumination and thereafter every 30 min until the end of the photodegradation process. The photocatalyst was separated from the dispersion by centrifugation (12,000 rpm, 20 min). Changes in the absorbance of dye molecules (RB or MB) in supernatant were mea-

sured on Evolution 600 spectrophotometer – Thermo Scientific at  $\lambda = 554 \text{ nm}$  and  $\lambda = 664 \text{ nm}$  for RB and MB, respectively.

## 3. Results and discussion

### 3.1. Structural, optical and morphological properties of carbonized PANI/TiO $_2$ nanocomposites

In order to study the influence of high temperature during the carbonization process on molecular structure of PANI component, to confirm the presence of TiO $_2$  NPs in TPC nanocomposites, and to reveal the possible changes in the crystalline structure of TiO $_2$  NPs, Raman spectroscopy was applied. Raman spectra of carbonized TPC-50 nanocomposite and precursor non-carbonized TP-50 nanocomposite, for comparison, are shown in Fig. 1.

In the Raman spectrum of TP-50 nanocomposite sample, Fig. 1a, bands characteristic for emeraldine salt form of PANI are observed at:  $1598$ ,  $1513$ ,  $1345$  and  $1172 \text{ cm}^{-1}$  [14,38]. The band at  $1598 \text{ cm}^{-1}$  can be assigned to the C=C stretching vibrations of the quinonoid rings, and/or C=C stretching vibrations of the semiquinonoid rings ( $\sim$  denotes the bond intermediate between the single and double bond). The band at  $1513 \text{ cm}^{-1}$  was attributed to the N–H bending vibration of protonated amine while the band at  $1345 \text{ cm}^{-1}$  was ascribed to the C–N $^{+}$  stretching vibration of polaronic structures [38]. Less intensive band at  $1172 \text{ cm}^{-1}$  was assigned to the C–H bending in-plane vibration of semiquinonoid rings in polaronic structures [38]. The bands observed at  $1569$ ,  $1410$  and  $617 \text{ cm}^{-1}$  in the Raman spectrum of sample TP-50 can be associated with the presence of substituted phenazine structural units, known to be crucial for the formation of PANI nanostructures [38–42].

The shoulder at  $1633 \text{ cm}^{-1}$  corresponds to the C=C stretching vibrations of benzenoid units, but also there is a possibility for the contribution of substituted phenazine units [38,40]. The presence of anatase TiO $_2$  NPs in TP-50 nanocomposite sample was confirmed by appearance of characteristic bands at  $155$ ,  $421$  and  $617 \text{ cm}^{-1}$  [14,43]. The strong band at  $155 \text{ cm}^{-1}$  was assigned to the  $E_g$  phonon mode, while the bands at  $421$  and  $617 \text{ cm}^{-1}$  are assigned as  $B_{1g}$  and  $E_g$  modes of the anatase phase, respectively [43–45].

Recently, we pointed out the significance of the existence of phenazine-containing oligoaniline nucleates for interaction of PANI chains and TiO $_2$  NPs through free-electron coupling on nitrogen atoms [46]. The protonated oligoaniline nucleates represented the initiation center for further polymerization process in the presence of positively charged colloidal TiO $_2$  NPs ( $\text{Ti-OH}_2^+$ ) at pH 3 [47]. Graphical illustration for these interactions is given on Fig. 1c.

The Raman spectrum of carbonized nanocomposite sample, TPC-50, is shown in Fig. 1b. The complex structure of the spectrum, characteristic for nanocomposite before carbonization (TP-50), completely disappeared. These changes in spectral features indicated significant structural changes in PANI molecules caused by high-temperature treatment. In the Raman spectrum of sample TPC-50, two broad bands, at  $1584 \text{ cm}^{-1}$  and at  $1351 \text{ cm}^{-1}$ , were observed. Band at  $1584 \text{ cm}^{-1}$ , also known as graphitic, G band, is a consequence of the stretching vibrations of any pair of  $sp^2$  atoms in both aromatic rings and chains. The G band is assigned to the  $E_{2g}$  phonon of  $sp^2$  bond of carbon atoms [15–22,48,49]. On the other hand, disorder-induced D band at  $1351 \text{ cm}^{-1}$  was assigned to the breathing vibrations of  $sp^2$  sites only in six-fold aromatic rings, not in chains [48,49] and  $A_{1g}$  mode [50]. It is well known that perfectly ordered single-crystal graphite shows only the G band in Raman spectrum [15–22,49,51]. Degree of disorder of two-dimensional  $sp^2$  structured carbonaceous materials could be obtained from the intensity ratio of the D ( $I_D$ ) and G bands ( $I_G$ ). Generally, an  $I_D/I_G$  ratio can be increased in two cases: when the amount of “disorganized carbon” increases, or when the size of graphite crystallite decreases

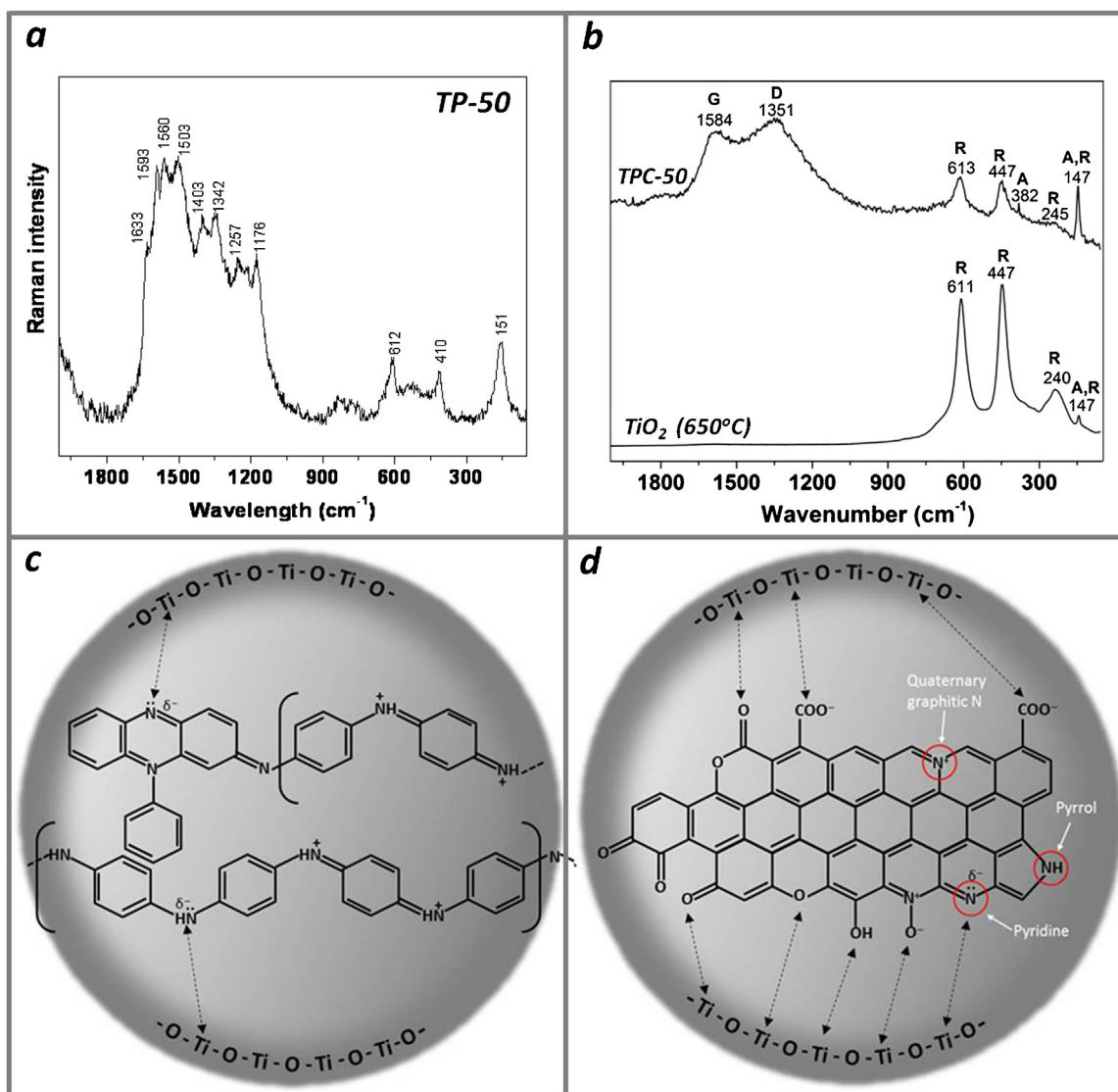


**Fig. 1.** Raman spectra of TP-50 nanocomposite (a), TPC-50 nanocomposite (b) and bare TiO<sub>2</sub> NPs calcined at 650 °C (b); Schematic presentations of possible interactions between TiO<sub>2</sub> NPs and PANI before carbonization (c) and after carbonization (d).

(followed with a break of the long-size periodicity) [49,51]. In our case,  $I_D/I_G$  ratio for TPC-50 was found to be  $\sim 2.2$ , pinpointing the significant disorder as a possible consequence of the nitrogen and oxygen atoms incorporation in the carbon  $sp^2$  network structure and reduced crystallite size [52]. Imperfections in molecular structure of carbonaceous materials can cause significant changes in their electronic structure, band gap, work function, optical properties, and conductivity [15]. These changes further have an influence on photoinduced charge transfer in TPC nanocomposites, i.e., their photocatalytic activity.

It is known that the carbonization of PANI, in general, causes the appearance of three different types of N atom-containing functional groups in the resulting structure: pyridine-like (denoted as N-6), pyrrole-like (N-5) and graphitic (quaternary) N (N-Q), Fig. 1d (marked in red), similar to nitrogen-doped 1-D carbonaceous nanostructures (e.g. carbon nanotubes, graphene...) [15–22,53]. Also, during the carbonization process, the oxygen containing species (carboxyl group, ketone, quinone, phenol, pyrene ether, and pyridine oxide) could be created on the surface of carbonized PANI, Fig. 1d, [15–22,53,54] opening the possibility for more efficient interaction with TiO<sub>2</sub> NPs [55–57]. Moreover, Li and coworkers find

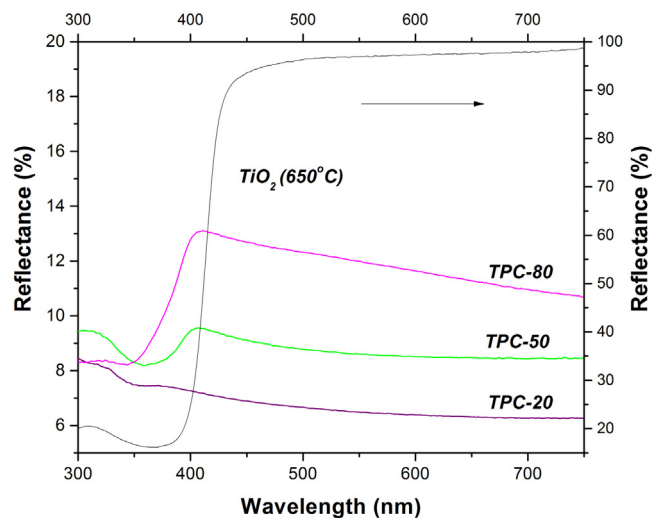


**Fig. 2.** Reflectance spectra of TPC nanocomposite samples and bare TiO<sub>2</sub> NPs calcined at 650 °C.



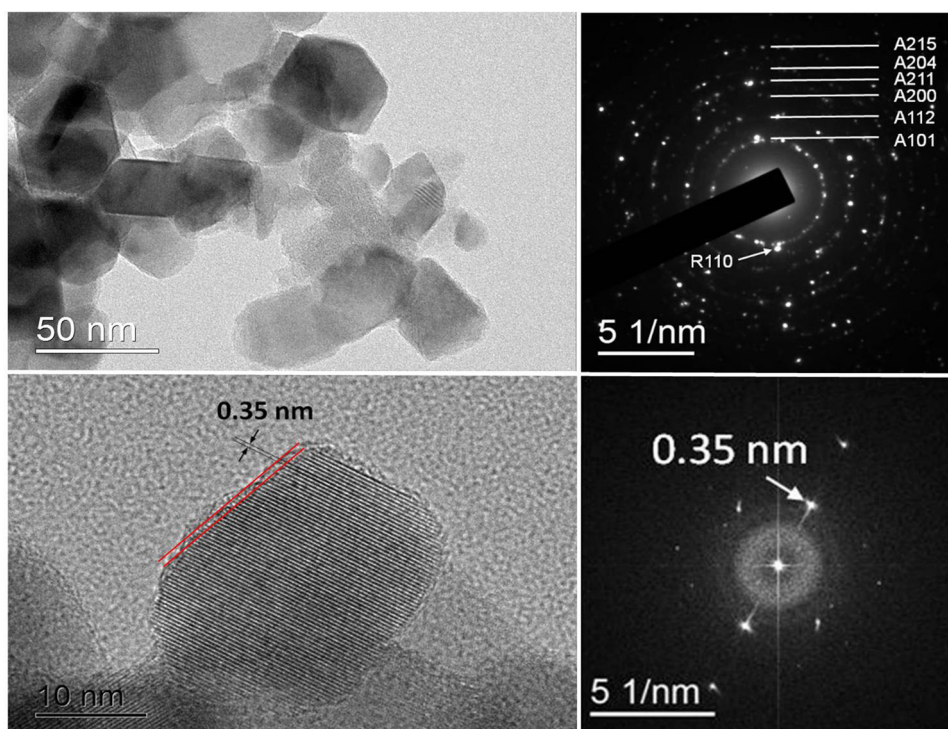


**Fig. 3.** TEM image of TPC-80 nanocomposite sample (a), the corresponding SAED pattern (b), TEM image at higher magnification of representative anatase  $\text{TiO}_2$  NP (c) and the corresponding FFT pattern (d).

a possibility for Ti—O—N and Ti—O—C interactions between  $\text{TiO}_2$  NPs and N and O atoms in carbonized structures [58].

Taking all these facts into account (changes in Raman spectra (Fig. 1b), surface structure of  $\text{TiO}_2$  NPs and functionalities of carbonized PANI) the possible interactions between  $\text{TiO}_2$  NPs and carbonized PANI in nanocomposites might be presented as in Fig. 1d.

During the carbonization of PANI at  $650^\circ\text{C}$ , some changes in the crystalline structures of  $\text{TiO}_2$  NPs also could be expected [59] and are, indeed, observed. Namely, in the Raman spectrum of TPC-50 nanocomposite sample, the appearance of the bands at  $147\text{ cm}^{-1}$  ( $E_g$  phonon mode) and  $382\text{ cm}^{-1}$  ( $B_{1g}$  mode) confirmed the presence of anatase crystalline phase [44,46]. Also, the new bands that appeared at  $613$ ,  $447$ ,  $245$  and  $147\text{ cm}^{-1}$  can be assigned to  $A_{1g}$ ,  $E_g$ , second-order (two-phonon) scattering and  $B_{1g}$  modes of rutile crystalline phase, respectively, formed by temperature induced phase transformation in  $\text{TiO}_2$  component of the nanocomposite [44,45,60,61]. The band at  $147\text{ cm}^{-1}$  is formed by mixed contributions of rutile  $B_{1g}$  mode and anatase  $E_g$  mode.

In order to elucidate the changes in crystalline structure of bare  $\text{TiO}_2$  NPs under the same conditions as in the process of carbonization, the Raman spectrum of bare  $\text{TiO}_2$  NPs calcined at  $650^\circ\text{C}$  in an inert atmosphere, is measured, Fig. 1b. Strong bands characteristic of the rutile crystalline phase are easy to observe at wavenumbers  $611$ ,  $447$  and  $240\text{ cm}^{-1}$ , while there is no noticeable presence of the most characteristic bands of anatase at  $155$  and  $630\text{ cm}^{-1}$  [43]. This result revealed the influence of carbonization process and PANI layer on the surface of  $\text{TiO}_2$  NPs on the crystalline structure of  $\text{TiO}_2$ , as the Raman spectrum of TPC-50 sample already implied.

Optical properties of TPC nanocomposites and bare  $\text{TiO}_2$  NPs calcined at  $650^\circ\text{C}$  in an inert atmosphere were studied by UV–vis spectroscopy in reflectance mode, Fig. 2. Absorption buildup at  $415\text{ nm}$  observed in the reflectance spectrum of calcined bare  $\text{TiO}_2$  NPs corresponds to band gap energy of  $\sim 3\text{ eV}$  and points to the appearance of rutile crystalline structure. Increase of absorbance

in the visible part of the spectra of TPC nanocomposites is in accordance with the increase of initial  $[\text{TiO}_2]/[\text{ANI}]$  mole ratio. It is known that introduction of the carbon phase into the  $\text{TiO}_2$  matrix led to an increase in absorbance in visible spectral region, which is proportional to carbon content in composite [62]. It was reported that the increase of absorbance could be the result of an increment of surface electric charge of the metal oxide, due to introduction of the carbonaceous form in the composite [63,64], or formation of an electronic interaction between the carbon and metal oxide phases [62,65–67]. The bands which appeared around  $\lambda = 350\text{ nm}$  in reflectance spectra of TPC nanocomposites are probably related to  $\pi$  electron transition in oxygen-containing carbonaceous structures, i.e.,  $n \rightarrow \pi^*$  transition of the  $\text{C}=\text{O}$  bond [68]. The observed shifting of their positions could be related to different concentrations of N in TPC nanocomposite samples [69].

Conventional bright field TEM images of nanocomposite sample TPC-80 at different magnifications and corresponding selected-area electron diffraction (SAED) pattern are shown in Fig. 3. The overall increase of dimensions of  $\text{TiO}_2$  NPs ( $d \sim 20\text{ nm}$ ) after thermal treatment of nanocomposites at  $650^\circ\text{C}$ , in comparison to dimensions of precursor colloidal  $\text{TiO}_2$  NPs ( $d \sim 4.5\text{ nm}$ ) was observed, Fig. 3a [33–47]. Spotty ring SAED pattern, Fig. 3b, indicated presence of anatase and rutile crystalline structures in polynanocrystalline TPC-80 sample. Also, uniformly deposited layer (marked by red lines) of carbonized PANI with a thickness of  $0.6$ – $0.7\text{ nm}$ , on the surface of  $\text{TiO}_2$  NP is clearly seen in TEM image obtained using higher magnification, Fig. 3c (marked by arrows). Quantitative analysis of TEM image using fast-Fourier-transform (FFT) operations, Fig. 3d, revealed lattice spacing value of  $0.35\text{ nm}$  characteristic for  $[101]$  direction of anatase  $\text{TiO}_2$  [70].

Unlike the single- and multi-wall carbon nanotubes [15], the carbonaceous layer on the surface of  $\text{TiO}_2$  NPs does not possess a high level of structural perfection, which is confirmed by the obtained  $I_D/I_G$  ratio of  $\sim 2.2$ . For more detailed examination of the impact of carbonization process on the crystalline structure of  $\text{TiO}_2$

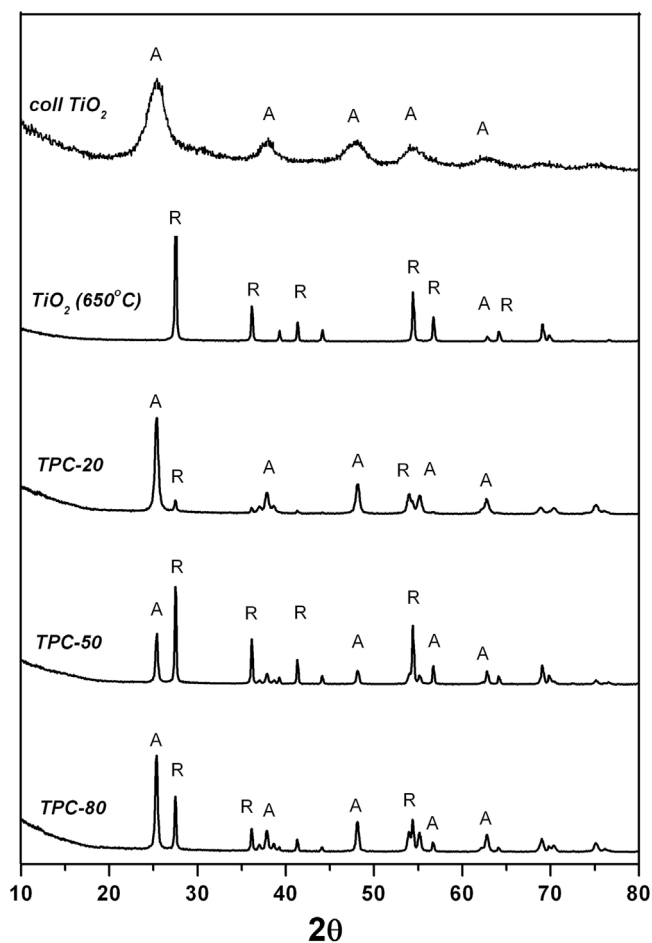


**Fig. 4.** XRD patterns of colloidal  $\text{TiO}_2$  NPs before and after calcination at  $650^\circ\text{C}$ , and nanocomposite samples TPC-20, TPC-50, and TPC-80.

NPs, TPC nanocomposites were synthesized with three different initial  $[\text{TiO}_2]/[\text{ANI}]$  mole ratios (20, 50 and 80) and XRD measurements were carried out.

The XRD patterns of precursor colloidal  $\text{TiO}_2$  NPs, calcined bare  $\text{TiO}_2$  NPs and TPC nanocomposites are shown in Fig. 4. XRD pattern of colloidal  $\text{TiO}_2$  NPs confirmed the existence of homogeneous anatase crystalline phase without peaks that could indicate the presence of a rutile polymorph of  $\text{TiO}_2$  [43]. Relative broadening of diffraction peaks of colloidal  $\text{TiO}_2$  NPs, as a consequence of their dimensions ( $d \sim 4.5$  nm), was observed. On the other hand, in the XRD pattern of bare  $\text{TiO}_2$  NPs calcined at  $650^\circ\text{C}$  only the peaks characteristic for rutile crystalline structure of  $\text{TiO}_2$  are observed.

According to the XRD patterns, Fig. 4, all TPC nanocomposites had been confirmed to be primarily a mixture of anatase and rutile crystalline structures. Diffraction peaks located at  $2\theta = 25.4^\circ, 37.8^\circ, 48.0^\circ, 54.5^\circ, 62.2^\circ$  are characteristic for the (101), (004), (200), (105) and (204) planes of the anatase phase (JCPDS 21-1272). While, the peaks located at  $27.5^\circ, 36.1^\circ, 54.4^\circ$  are characteristic for the (110), (101), (211) planes of the rutile phase (JCPDS 21-1276). Rutile crystalline phase appeared in all TPC nanocomposites, independently of the amount of carbonized PANI. This finding is in agreement with Raman spectroscopy measurements shown in Fig. 1 which implied that carbonization process significantly affecting the primary crystalline structure of  $\text{TiO}_2$  NPs. The absence of diffraction peaks characteristic for carbonized PANI structures in XRD patterns of synthesized nanocomposites indicated their low content, which is otherwise expected, due to low initial ANI/ $\text{TiO}_2$  mole ratio. Also,

the formation of TiN compound in nanocomposite samples as a result of heating to  $650^\circ\text{C}$  was not observed.

The crystalline compositions of  $\text{TiO}_2$  NPs in TPC-20, TPC-50 and TPC-80 nanocomposites and bare  $\text{TiO}_2$  NPs calcined at  $650^\circ\text{C}$  are listed in Table 2. Taking into account that the reaction conditions during the carbonization process were the same for all synthesized samples, the main reason for various anatase to rutile ratios obtained in nanocomposites could be found in different initial  $\text{TiO}_2/\text{ANI}$  mole ratios. Such differences probably led toward different thicknesses of carbonized PANI layer on the surfaces of  $\text{TiO}_2$  nanoparticles, which finally affect heat flow and the crystalline structure of  $\text{TiO}_2$ . Namely, the lowest percentage of rutile detected in the sample TPC-20 corresponds to the highest amount of ANI in the initial reaction mixture and the highest percentage of nitrogen in the sample after carbonization (0.306% of nitrogen, 1.821% of carbon, obtained by elemental analysis). On the other hand, the elemental analysis revealed the lowest concentration of nitrogen (0.096%) and carbon (0.970%) in the sample TPC-50, pointing to the possibly lowest amount of formed carbonized PANI which can be consistent with the observed highest percentage of rutile phase (Table 2). In the sample TPC-80 the concentrations of nitrogen and carbon were 0.218% and 1.459%, respectively.

Previous conclusions concerning the influence of carbonized PANI layer on crystalline structures of  $\text{TiO}_2$  NPs are in accordance with XRD results on the existence of only rutile crystalline structure (99%) in bare  $\text{TiO}_2$  NPs thermally treated under the same conditions ( $650^\circ\text{C}$ , an inert atmosphere) as the TPC samples (Table 2). Also one should not forget the potential influence of morphology and molecular structure of PANI in nanocomposites before carbonization, on the anatase/rutile ratio.

The morphological changes of TPC nanocomposite samples were followed by SEM. SEM micrographs and corresponding EDS spectra of the TPC samples are presented in Fig. 5. SEM micrographs reveal that the degree of agglomeration decreases in direction from the sample TP-20 to the sample TP-80. Elemental mapping of Ti on the surface of TPC samples performed in EDS mode confirmed homogeneous distribution of Ti on each tested place. Homogeneous distribution of Ti implies homogeneous distribution of  $\text{TiO}_2$  NPs in surface layer of TPC nanocomposites. Nearly the same weight percentage of Ti in all composites observed in EDS (Fig. 5) is in agreement with the same initial concentration of  $\text{TiO}_2$  NPs used in the synthesis of each sample.

TGA (Fig. S1) revealed that the amounts of  $\text{TiO}_2$  NPs in TPC nanocomposites vary in the range 96–98.5 w%, which are in accordance with EDS measurements. Consequently, the content of carbonized PANI in TPC nanocomposites was in the range 1.5–4 w%.

### 3.2. Adsorption capacity and photocatalytic activity of TPC nanocomposites

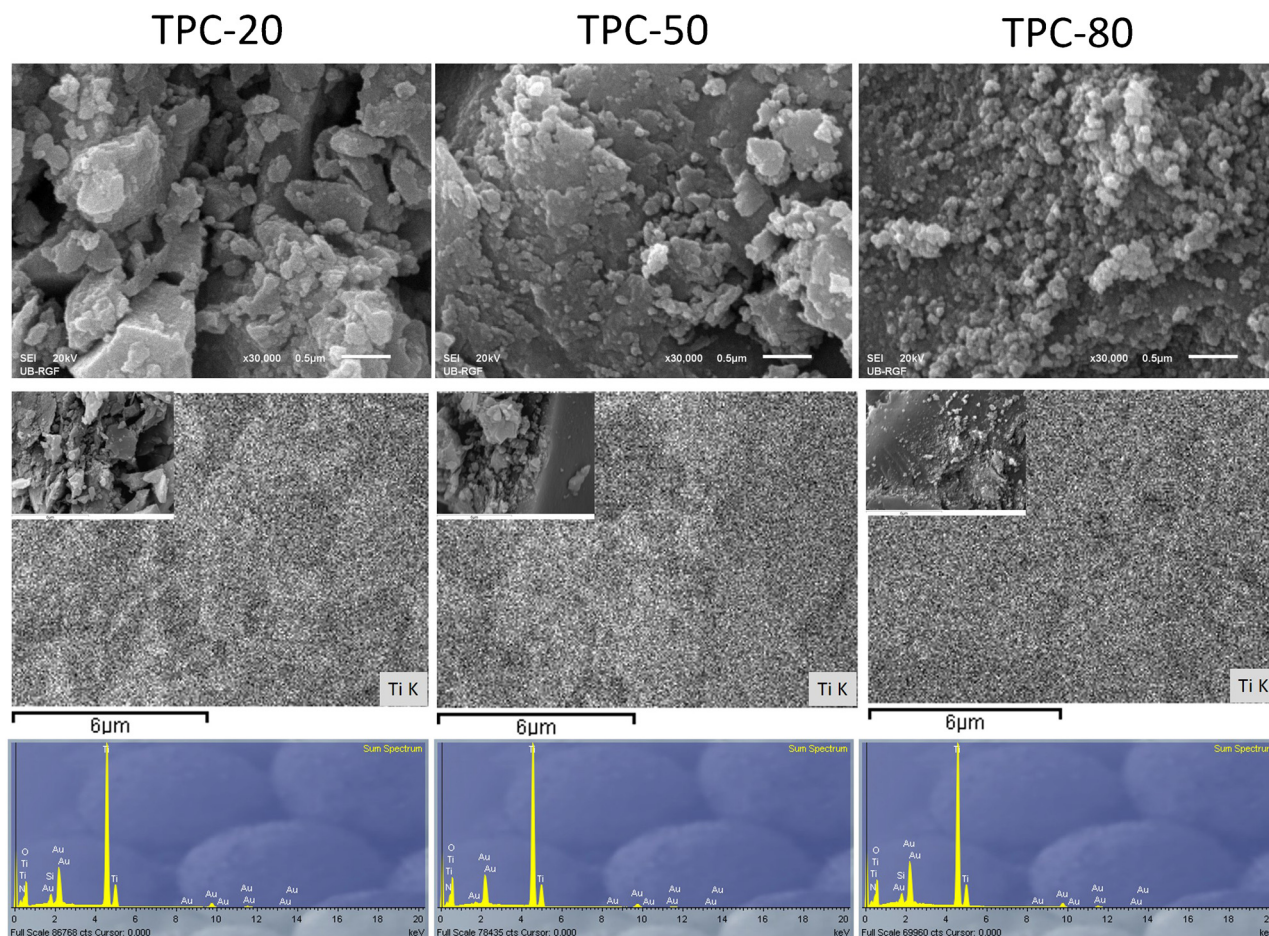
The photocatalytic activities of TPC nanocomposites with different initial  $\text{TiO}_2/\text{aniline}$  mole ratio (TPC-20, TPC-50 and TPC-80) were tested in degradation processes of model molecules MB and RB in oxygen atmosphere and under white light illumination. In our previous work we have shown that non-carbonized PANI/ $\text{TiO}_2$  nanocomposites with  $\text{TiO}_2/\text{aniline}$  mole ratio in range from 50 to 150 removed only 20–57% of MB within 6 h of white-light illumination, while the degradation efficiency of RB was in the range 48–96% for the same period (Fig. S2). It was expected that carbonization of PANI/ $\text{TiO}_2$  nanocomposites will improve photoinduced charge separation, which consequently will lead toward generally a more efficient photocatalytic system.

The TPC nanocomposites contain different adsorption sites for MB and RB molecules, whose nature and number define the adsorption potential of each of them. In order to analyze the adsorption process of MB and RB on the surface of TPC-20, TPC-50 and TPC-80



**Table 2**The crystalline compositions of bare TiO<sub>2</sub> NPs and TiO<sub>2</sub> NPs in TPC nanocomposites.

Sample	TiO <sub>2</sub> coll	TiO <sub>2</sub> (650 °C)	TPC-20	TPC-50	TPC-80
TiO <sub>2</sub> /ANI molar ratio	–	–	20	50	80
Anatase (%)	100	1	90	34	62
Rutile (%)	0	99	10	66	38

**Fig. 5.** SEM images of TPC nanocomposite samples and corresponding elemental mapping of Ti (second row, bright spots).

nanocomposites, adsorption isotherms after 30 min equilibration in the dark were determined (Fig. 6).

Both, MB and RB adsorption isotherms followed the Langmuir model, i.e., the amounts of the adsorbed dyes increased regardless of which TPC nanocomposites was used [71]. The Langmuir isotherm constants were obtained for both dyes by the method of the least-squares fitting applied to the plot (graphic) based on equation:

$$1/Q_e = 1/Q_{\max} + 1/K_{\text{obs}}Q_{\max}C_e$$

where  $Q_e$  (mg/g) is the amount of MB (or RB) adsorbed per unit mass of carbonized PANI/TiO<sub>2</sub> nanocomposites,  $Q_{\max}$  (mg/g) is the maximum adsorbed quantity of MB (or RB) i.e. maximum adsorption capacity,  $C_e$  is the concentration of unadsorbed MB (or RB) in solution at the adsorption equilibrium,  $K_{\text{obs}}$  is the adsorption constant in the dark related to the affinity of the binding sites (L/mg).

The determined values for adsorption constants ( $K_{\text{obs}}$ ) of MB and RB and maximum adsorption capacities ( $Q_{\max}$ ) of nanocomposites are listed in Table 3.

The maximum quantity of MB was adsorbed on nanocomposite sample TPC-50 ( $Q_{\max} = 2.533$  mg/g) despite the fact that values

for pores volume ( $0.095$  cm<sup>3</sup>/g, Fig. S3) and specific surface area ( $S_{\text{BET}} = 18$  m<sup>2</sup>/g, Fig. S3) were the smallest of all tested nanocomposites. Also, the value of adsorption constant in the dark was the highest for the sample TPC-50 ( $K_{\text{obs}} = 0.721$  L/mg) followed by samples TPC-80 ( $K_{\text{obs}} = 0.675$  L/mg) and TPC-20 ( $K_{\text{obs}} = 0.135$  L/mg). These measurements revealed that the adsorption capacity is not correlated with the variation in surface area of TPC nanocomposites taking into account that  $S_{\text{BET}}$  values, of samples TPC-20 and TPC-80 were  $35$  m<sup>2</sup>/g and  $21$  m<sup>2</sup>/g, respectively.

The adsorption efficiencies of RB on TPC nanocomposites were generally lower compared with MB. The determined values for adsorption constants ( $K_{\text{obs}}$ ) of RB and maximum adsorption capacities ( $Q_{\max}$ ) of nanocomposites are listed in Table 3.

The  $Q_{\max}$  values for adsorption properties of RB were in range of  $0.573$ – $0.998$  mg/g (Table 3). The maximum quantity of RB was adsorbed on the sample TPC-80 ( $Q_{\max} = 0.998$  mg/g). In the case of RB, the adsorption constant was the highest for the sample TPC-50 ( $K_{\text{obs}} = 1.556$  L/mg).

The study of the adsorption properties for both dyes pointed to the existence of a different affinity of binding sites in TPC nanoco-

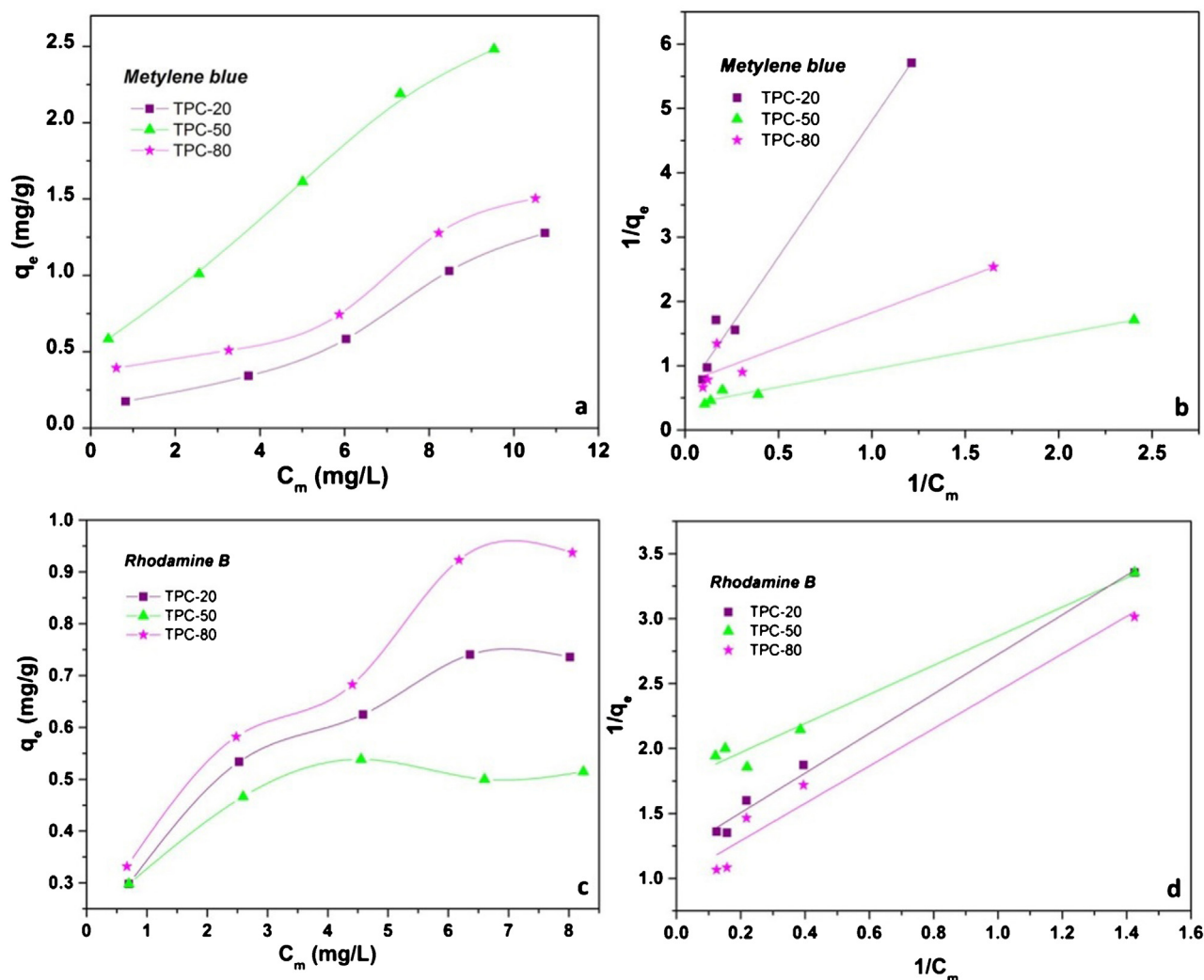


Fig. 6. Adsorption isotherms of Methylene blue and Rhodamine B after 30 min equilibration in the dark.

**Table 3**  
Adsorption properties of MB and RB in the dark and kinetic data of their photocatalytic degradations in the presence of TPC nanocomposites.

Sample	Methylene blue (MB)				Rhodamine B (RB)			
	$1/Q_{\max}$	$Q_{\max}$ (mg/g)	$K_{\text{obs}}$	$k_{\text{app}}$	$1/Q_{\max}$	$Q_{\max}$ (mg/g)	$K_{\text{obs}}$	$k_{\text{app}}$
TPC-20	0.572	1.748	0.135	0.018	1.201	0.833	0.788	0.017
TPC-50	0.395	2.533	0.721	0.035	1.744	0.573	1.556	0.030
TPC-80	0.735	1.3601	0.675	0.078	1.002	0.998	0.696	0.033

moposite samples, and the adsorption efficiency definitely was not consistent with their surface area and pore volumes.

Fig. 7 shows the decrease in MB (Fig. 7a) and RB (Fig. 7b) concentrations versus illumination time in the presence of TPC-20, TPC-50 and TPC-80 nanocomposite samples, determined by UV–vis spectroscopy. The bare (colloidal)  $\text{TiO}_2$  NPs, used as reference sample in this study, under the same experimental conditions removed 2% of MB and 3% of RB from the solution after 60 min and 90 min of white light illumination, respectively. The bare  $\text{TiO}_2$  NPs calcined at  $650^\circ\text{C}$ , in an inert atmosphere, showed greater photocatalytic activities than the colloidal  $\text{TiO}_2$  NPs, as expected [59]. They removed 35% of MB and 22% of RB for the same time interval. The photolysis of MB and RB molecules was negligible, less than 1% after 6 h of irradiation [14].

The sample TPC-80, characterized by the lowest adsorption capacity ( $Q_{\max} = 1.360 \text{ mg/g}$ ), exhibited maximum photocatalytic

efficacy and already after 60 min the degradation of MB was finished, Fig. 7a. The sample TPC-50 removed 89% of MB after 60 min of illumination. It should be mentioned that the sample TPC-50 showed significantly higher photocatalytic efficiency in degradation of MB compared to non-carbonized PANI/ $\text{TiO}_2$  nanocomposite (Fig. S2) characterized with the same initial ratio of  $\text{TiO}_2$  and aniline (50:1). In the presence of non-carbonized PANI/ $\text{TiO}_2$  nanocomposite after 6 h of illumination only 57% of MB was removed from the solution (Fig. S2). Finally, the sample TPC-20 with highest specific surface area ( $S_{\text{BET}} = 35 \text{ m}^2/\text{g}$ ) has shown the lowest photocatalytic efficacy in degradation process of MB, Fig. 7a, which is probably associated with the smallest pore size ( $\sim 4 \text{ nm}$ ) in this sample compared to other samples.

The similar photocatalytic efficiencies of the TPC nanocomposites in the process of degradation of RB were observed, Fig. 7b. Namely, after 90 min, 80–96% of RB degraded. We men-



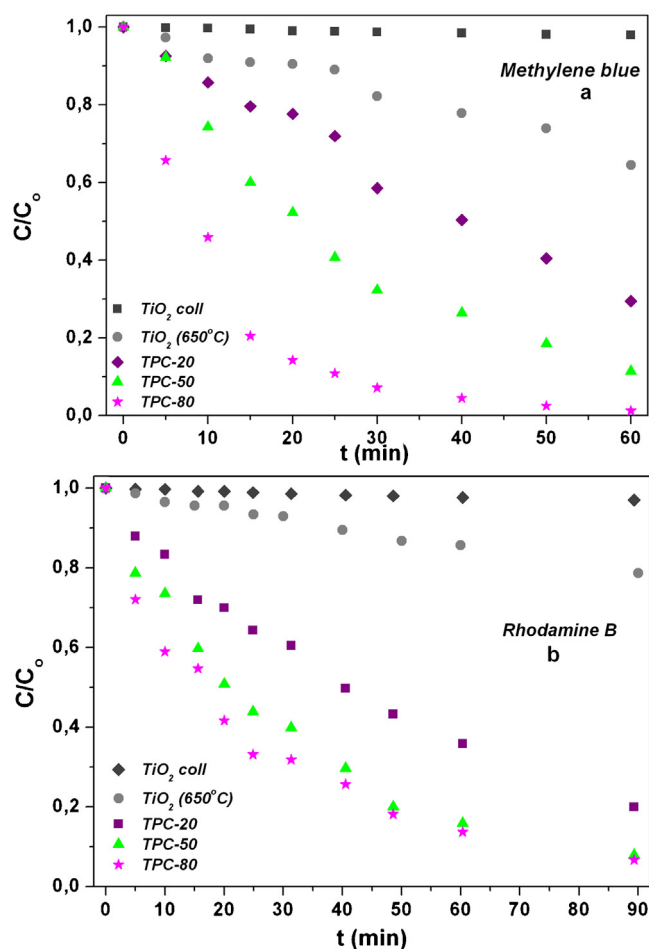


Fig. 7. Changes of relative concentrations of Methylene blue (a) and Rhodamine B (b) during the photodegradation in the presence of TPC nanocomposites and bare  $TiO_2$  NPs calcined at  $650^\circ C$ .

tion here that carbonization of PANI in PANI/ $TiO_2$  nanocomposites induced, again, a significant increase of the photocatalytic efficiency, as in the case of MB degradation. In our previous work [14], a PANI/ $TiO_2$  nanocomposite sample, which was the precursor for the synthesis of carbonized (TPC-50) sample in this study, degraded only 48% of RB after 6 h of illumination (Fig. S2) but after carbonization, 92% of RB degraded after 90 min. A slightly greater activity during degradation process of RB demonstrated sample TPC-80 (95%, after 90 min of illumination). The possible reason for similar photocatalytic efficiencies of TPC-50 and TPC-80 samples in RB degradation processes could be found in their comparable pore volumes ( $0.095$  and  $0.131 \text{ cm}^3/\text{g}$ , Fig. S3) which are almost two times larger compared to pore volume of TPC-20 sample ( $0.053 \text{ cm}^3/\text{g}$ , Fig. S3). Larger pore volumes allow easier access of RB molecules to the surface of TPC photocatalyst, taking into account their dimension and steric hindrance, which leads to greater efficiency of photocatalytic processes. On the other hand, for successful degradation of MB, the influence of pore size was less important compared with the influence of interactions between dye and photocatalyst. Namely, nitrogen in thiazine group of MB could ensure efficient hydrogen bonding interaction of  $N \cdots H-N$  type with H atom from  $-NH$  groups (e.g. from pyrrole type group) in TPC nanocomposites, particularly in the sample with highest percentage of nitrogen such as TPC-80 ( $0.3056\%$ ), which could also lead to greater overall photocatalytic efficiency. The observed dominant photocatalytic activities of the sample TPC-80 in degradation processes of both dyes, MB and RB, are in accordance with results of

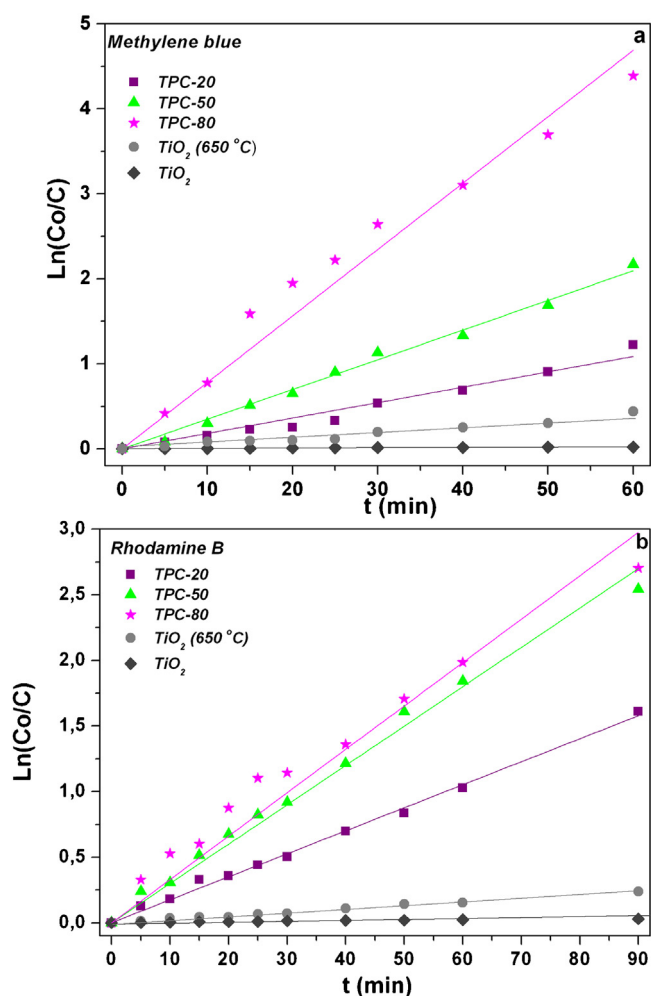


Fig. 8. Kinetic plots of degradation of Methylene blue (a) and Rhodamine B (b).

SEM characterization, Fig. 5, which indicated the lowest level of agglomeration in this sample.

Kinetic plots of degradation of MB and RB, Fig. 8a and b, where obtained using kinetic model which assumed that the low concentration of dye used in experiment i.e.  $K_{obs}C_e \ll 1$ , which further allowed the use of classical first order equation:

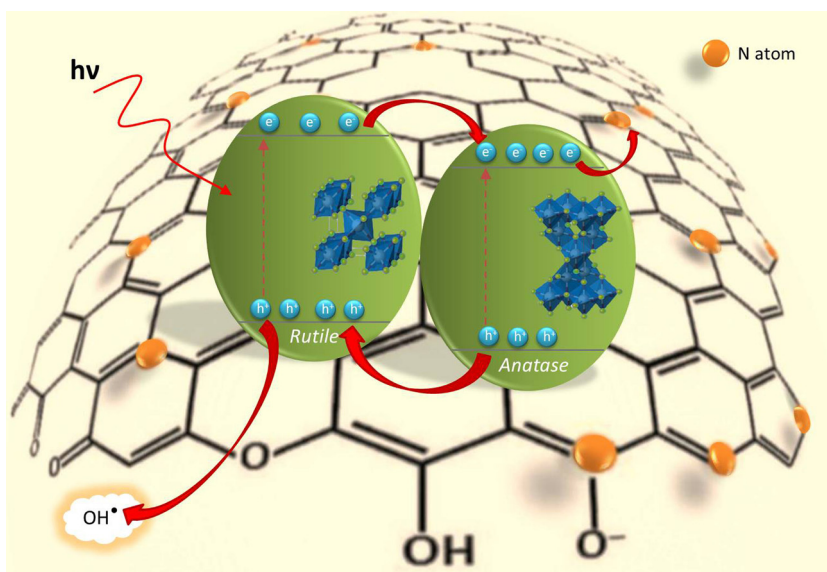
$$-dC/dt = k_{app}K_{obs}C_e$$

where  $k_{app}$  is rate constant,  $K_{obs}$  adsorption constant and  $C_e$  concentration.

Significantly slower degradations of MB and RB in the presence of bare  $TiO_2$  compared to their degradation rates in the presence of studied TPC nanocomposites is easy to see in Fig. 8a and b.

Also, a linear relationship is apparent between degradation rate constants ( $k_{app}$ ) of MB calculated from the first-order kinetics in the presence of TPC nanocomposite samples and initial  $TiO_2$ /aniline mole ratios. The reaction rate constants of MB removal via photocatalytic degradation increased from  $k_{app} = 0.018 \text{ min}^{-1}$  for nanocomposite sample TPC-20 to  $k_{app} = 0.078 \text{ min}^{-1}$  for sample TPC-80 (Table 3). The reaction rate constants of RB removal increased from  $0.017 \text{ min}^{-1}$  for sample TPC-20 to  $0.033 \text{ min}^{-1}$  for sample TPC-80 (Table 3).

For the explanation of significantly improved photocatalytic activities of carbonized TPC nanocomposite samples compared to photocatalytic activities of precursor TP nanocomposites, changes in crystalline structures of  $TiO_2$  during carbonization process, and



**Scheme 1.** Photoinduced charge separation in TPC nanocomposites.

the increased charge separation in the carbonized structure, should be particularly taken into account.

It is well known that efficient charge separation in mixed-phase titania nanocrystals is the main reason for their high photocatalytic activity. In mixed-phase  $\text{TiO}_2$ , charges photoinduced by visible light on rutile phase are stabilized through electron transfer to lower energy anatase lattice trapping sites [72]. On that way, catalytic “hot spots” at the rutile-anatase interface created which led toward overall increase of titania photocatalytic activity.

In addition, more efficient photoinduced charge separation in TPC nanocomposites, which led toward their better photocatalytic activity compared to non-carbonized PANI/ $\text{TiO}_2$  nanocomposites and bare precursor anatase  $\text{TiO}_2$  nanoparticles, can also be explained by the existence of nitrogen in such carbonized nanostructures (Scheme 1). Namely, some previous studies have indicated that nitrogen doping of carbonized systems affects their electronic structures which is reflected in great enhancement of conductivity as a consequence of the recovery of the  $sp^2$  graphene network possibly disrupted by the presence of defects (disrupted conjugation sites, vacancies, etc.) [73].

Generally, graphene-like carbonaceous materials in contact with metal-oxide semiconductors are known as excellent electron acceptors and transporters, which could improve their overall photocatalytic performances by reducing the recombination of the photogenerated electron-hole pairs. The existence of nitrogen in

carbonaceous structure increases the electronic density of states near the Fermi level, thus creating conditions for efficient electron transfer from  $\text{TiO}_2$  nanocrystals [74] and prolonging the lifetime of holes, which eventually can lead to a more efficient photocatalytic process. The presence of nitrogen in carbonized structure such as TPC nanocomposites provides additional anchor sites for  $\text{TiO}_2$  nanoparticles establishing close interfacial contact between carbonized PANI and  $\text{TiO}_2$ , and further stabilizing the nanocomposite system [75,76].

For photodegradation of both MB and RB in the presence of TPC nanocomposites, the rate constants ( $k_{\text{app}}$ ) were the greatest for the sample TPC-80. The reason for highest rate constants could be found in fact that sample TPC-80 contains 38% of the rutile phase. This amount of rutile is very close to its reported content in mixed phase  $\text{TiO}_2$ , which shows an excellent photocatalytic activity in the degradation processes of test molecules [77,78]. For comparison, it should be mentioned that the reaction rate constants ( $k_{\text{app}}$ ) of the MB and RB photodegradations in the presence of the precursor colloidal anatase  $\text{TiO}_2$  nanocrystals ( $d \sim 4.5 \text{ nm}$ ) were two orders of magnitude lower,  $k_{\text{app}(\text{MB})} = 2.1 \times 10^{-4} \text{ min}^{-1}$  and  $k_{\text{app}(\text{RB})} = 7.3 \times 10^{-4} \text{ min}^{-1}$ , while in the presence of calcined  $\text{TiO}_2$  NPs were almost order of magnitude lower,  $k_{\text{app}(\text{MB})} = 6.5 \times 10^{-3} \text{ min}^{-1}$  and  $2.7 \times 10^{-3} \text{ min}^{-1}$ .

The possibility of multiple use of the photocatalyst is highly desirable. Fig. 9 shows removal efficiency of MB and RB dyes in the

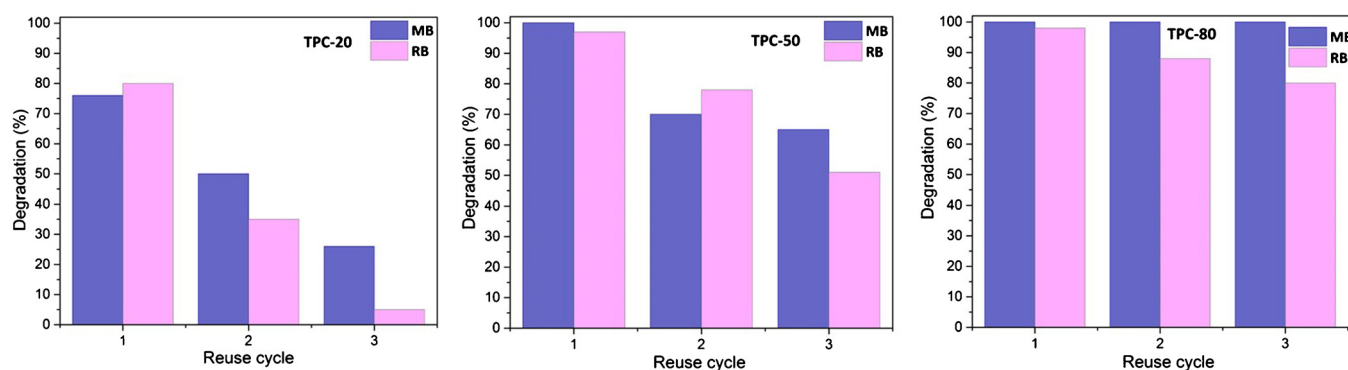


**Fig. 9.** Methylene blue and Rhodamine B removal efficiencies in the presence of TPC nanocomposites (10 mg/mL) after three cycles of illumination (60 min of illumination for MB and 90 min of illumination for RB, initial dye concentrations:  $1 \times 10^{-5} \text{ mol/L}$ ).

presence of the same amount of TPC nanocomposites during three photodegradation cycles. In other words, the same samples were used in fresh batch of dye solution and illuminated three times. Samples TPC-20 and TPC-50 showed significantly lower removal efficiency after the second and third cycles for both dyes in selected time intervals (60 min for MB and 90 min for RB). On the other hand, the photocatalytic removal degree of MB in the presence of TPC-80 nanocomposite is retained at remarkably high level after three cycles of illumination indicating its chemical and photo stability. Slight decrease in the removal efficiency of RB in the presence of same nanocomposite sample after second and third cycles is observed.

#### 4. Conclusions

PANI/TiO<sub>2</sub> nanocomposites, synthesized at three different initial [TiO<sub>2</sub>]/[ANI] molar ratios (20, 50 and 80) were carbonized at 650 °C to obtain nanocomposites of carbonized PANI and TiO<sub>2</sub>. These novel nanocomposites were further characterized by several techniques and explored as photocatalysts. Raman spectroscopy measurements of carbonized PANI/TiO<sub>2</sub> nanocomposites pointed to significant temperature-induced changes in molecular structure of PANI, by the appearances of G and D bands, assigned to stretching and breathing vibrations of sp<sup>2</sup> sites. Also, Raman spectroscopy and XRD revealed the presence of the anatase phase and newly-formed rutile phases in all carbonized PANI/TiO<sub>2</sub> nanocomposites, while in the bare TiO<sub>2</sub> NPs, thermally treated under the same experimental conditions, only rutile phase (99%) is detected. This finding suggests that the carbonization process and PANI layer on the surface of the TiO<sub>2</sub> NPs have a great effect on their crystalline structure. The initial [TiO<sub>2</sub>]/[ANI] mole ratio has a significant impact on the anatase to rutile crystalline ratio in carbonized PANI/TiO<sub>2</sub> composites. Carbonized PANI layer was observed on the surface of TiO<sub>2</sub> nanocrystals. The carbonization process induced a significant increase of the photocatalytic efficiencies of nanocomposites. The sample TPC-50 already after 60 min degraded almost 90% of MB, showing considerably higher efficiency compared to non-carbonized PANI/TiO<sub>2</sub> (6 h was needed for degradation of 57% MB) and bare colloidal TiO<sub>2</sub> nanoparticles. Similar improvement in photocatalytic behavior of carbonized PANI/TiO<sub>2</sub> nanocomposites is detected using the model molecule RB: sample TPC-50 degraded 92% of RB after 90 min, while the non-carbonized precursor composite sample was able to degrade less than 50% for 6 h. It has been shown that the increase of the initial [TiO<sub>2</sub>]/[ANI] molar ratio (sample TPC-80) induced a maximum efficiency in the degradation process of MB within one hour. The obtained results revealed that the carbonized PANI/TiO<sub>2</sub> nanocomposites have a great potential for application in photocatalytic degradation of organic pollutants. Also, there is large space for enhancement of their photocatalytic activity through changes in synthetic conditions (pH, type of acid dopant, etc.) of non-carbonized precursors and optimization of carbonization process that would lead to a better dispersion of nanocomposites i.e. lower degree of agglomeration. For the future work we plan to test efficiency of these nanocomposites in the degradation processes of other types of synthetic dyes (Acid, Direct and Reactive) taking into account enormous problem of non-degraded textile dyes in effluents and consequently in water-courses.

#### Acknowledgment

Financial support for this study was granted by The Ministry of Education, Science and Technological Development of The Republic of Serbia, Projects: OI 172056, OI 172043 and III45020.

#### Appendix A. Supplementary data

Supplementary data associated with this article can be found, in the online version, at <http://dx.doi.org/10.1016/j.apcatb.2017.05.023>.

#### References

- [1] M. Ni, M.K.H. Leung, D.Y.C. Leung, K. Sumathy, *Renew. Sust. Energy Rev.* 11 (2007) 401–425.
- [2] A. Fujishima, X. Zhang, D.A. Tryk, *Chem. Rev.* 63 (2008) 515–582.
- [3] U. Riaz, S.M. Ashraf, J. Kashyap, *Polym.-Plast. Technol.* 54 (2015) 1850–1870.
- [4] U. Riaz, S.M. Ashraf, J. Kashyap, *Mater. Res. Bull.* 71 (2015) 75–90.
- [5] K.R. Reddy, M. Hassan, V.G. Gomes, *Appl. Catal. A: Gen.* 489 (2015) 1–16.
- [6] M.A. Islam, T.K. Purkait, M.H. Mobarok, I.M.D. Hoehlein, R. Sinelnikov, M. Iqbal, D. Azulay, I. Balberg, O. Millo, B. Rieger, J.G.C. Veinot, *Angew. Chem.* 55 (2016) 7393–7397.
- [7] K.R. Reddy, K.P. Lee, A. I. Gopalan, *J. Nanosci. Nanotechnol.* 7 (2007) 3117–3125.
- [8] K.R. Reddy, B.C. Sin, K.S. Ryu, J.C. Kim, H. Chung, Y. Lee, *Synth. Met.* 159 (2009) 595–603.
- [9] Y.P. Zhang, S.H. Lee, K.R. Reddy, A.I. Gopalan, K.P. Lee, *J. Appl. Polym. Sci.* 104 (2007) 2743–2750.
- [10] K.R. Reddy, K.P. Lee, A.I. Gopalan, A.M. Showkat, *Polym. J.* 38 (2006) 349–354.
- [11] K.R. Reddy, K.P. Lee, Y. Lee, A.I. Gopalan, *Mater. Lett.* 62 (2008) 1815–1818.
- [12] K.R. Reddy, H.M. Jeong, Y. Lee, A.V. Raghu, *J. Polym. Sci. Polym. Chem. A* 48 (2010) 1477–1484.
- [13] C. Wang, L. Wang, J. Jina, J. Liu, Y. Li, M. Wu, L. Chen, B. Wang, X. Yang, B.L. Su, *Appl. Catal. B: Environ.* 188 (2016) 351–359.
- [14] M. Radoičić, Z. Šaponjić, I.A. Janković, G. Ćirić-Marjanović, S.P. Ahrenkiel, M.I. Comor, *Appl. Catal. B: Environ.* 136–137 (2013) 133–139.
- [15] G. Ćirić-Marjanović, I. Pašti, S. Mentus, *Prog. Mater. Sci.* 69 (2015) 61–182.
- [16] G. Ćirić-Marjanović, N. Pašti, A. Janošević, S. Mentus, *Chem. Pap.* 67 (2013) 781–813.
- [17] S. Mentus, G. Ćirić-Marjanović, M. Trchová, J. Stejskal, *Nanotechnology* 20 (2009) 10, 245601.
- [18] A. Janošević, I. Pašti, N. Gavrilov, S. Mentus, G. Ćirić-Marjanović, J. Krstić, J. Stejskal, *Synth. Met.* 161 (2011) 2179–2184.
- [19] N. Gavrilov, I.A. Pašti, M. Vujković, J. Travas-Sejdic, G. Ćirić-Marjanović, S.V. Mentus, *Carbon* 50 (2012) 3915–3927.
- [20] N. Gavrilov, I.A. Pašti, M. Mitrić, J. Travas-Sejdic, G. Ćirić-Marjanović, S.V. Mentus, *J. Power Sources* 220 (2012) 306–316.
- [21] D. Micić, B. Šljukić, Z. Žujović, J. Travas-Sejdic, G. Ćirić-Marjanović, *Electrochim. Acta* 120 (2014) 147–158.
- [22] G. Ćirić-Marjanović, S. Mentus, I. Pašti, N. Gavrilov, J. Krstić, J. Travas-Sejdic, L.T. Stover, J. Kopecká, Z. Moravková, M. Trchová, J. Stejskal, *J. Phys. Chem. C* 118 (2014) 14770–14784.
- [23] N. Gavrilov, M. Dašić Tomić, I. Pašti, G. Ćirić-Marjanović, S. Mentus, *Mater. Lett.* 65 (2011) 962–965.
- [24] M. Mališić, A. Janošević, B. Šljukić Paunković, I. Stojković, G. Ćirić-Marjanović, *Electrochim. Acta* 74 (2012) 158–164.
- [25] J. Milikić, G. Ćirić-Marjanović, S. Mentus, D.M.F. Santos, C.A.C. Sequeira, B. Šljukić, *Electrochim. Acta* 213 (2016) 298.
- [26] Z.R. Tang, F. Li, Y.H. Zhang, X.Z. Fu, Y. Xu, *J. Phys. Chem. C* 115 (2011) 7880–7886.
- [27] M. Zhu, P. Chen, M. Liu, *ACS Nano* 5 (2011) 4529–4536.
- [28] M. Zhu, P. Chen, M. Liu, *Langmuir* 28 (2012) 3385–3390.
- [29] V. Loípez, R.S. Sundaram, C. Gómez-Navarro, D. Olea, M. Burghard, J. Gómez-Herrero, F. Zamora, K. Kern, *Adv. Mater.* 21 (2009) 4683–4686.
- [30] L. Wang, L. Shen, L. Zhu, H. Jin, N. Bing, L. Wang, *J. Nanomater.* 794625 (2012) 7.
- [31] L. Wang, L. Shen, Y. Li, L. Zhu, J. Shen, L. Wang, *Int. J. Photoenergy* 824130 (2013) 7.
- [32] K.R. Reddy, V.G. Gomes, M. Hassan, *Mater. Res. Express* 1 (2014) 015012.
- [33] T. Rajh, D. Tiede, M. Thurnauer, *J. Non-Cryst. Solids* 207 (1996) 815.
- [34] R. Thompson, *Inorg. Chem.* 23 (1984) 1794–1798.
- [35] F. Rouquerol, J. Rouquerol, K.S.W. Sing, P. Llewellyn, G. Maurin, *Adsorption by powders and porous solids, in: Principles, Methodology and Applications*, Academic Press, New York, 2012.
- [36] B.C. Lippens, B.G. Linsen, J.H. de Boer, *J. Catal.* 3 (1964) 32.
- [37] K. Sing, D. Everett, R. Haul, L. Moscou, R. Pierotti, J. Rouquerol, T. Siemieniowska, *Pure Appl. Chem.* 57 (1985) 603–619.
- [38] G. Ćirić-Marjanović, M. Trchová, J. Stejskal, *J. Raman Spec.* 39 (2008) 1375–1380.
- [39] A. Janošević, G. Ćirić-Marjanović, B. Marjanović, P. Holler, M. Trchová, J. Stejskal, *Nanotechnology* 19 (2008) 8, 135606.
- [40] G. Ćirić-Marjanović, N.V. Blinova, M. Trchová, J. Stejskal, *J. Phys. Chem. B* 111 (2007) 2188–2199.
- [41] G. Ćirić-Marjanović, M. Trchová, E.N. Konyushenko, P. Holler, J. Stejskal, *J. Phys. Chem. B* 112 (2008) 6976–6987.
- [42] J.E. Pereira da Silva, D.L.A. de Faria, S.I. Córdoba de Torresi, M.L.A. Temperini, *Macromolecules* 33 (2000) 3077–3083.



- [43] M. Radoičić, Z. Šaponjić, J. Nedeljković, G. Ćirić-Marjanović, J. Stejskal, *Synth. Met.* 160 (2010) 1325–1334.
- [44] J. Zhang, M. Li, Z. Feng, J. Chen, C. Li, *J. Phys. Chem. B* 110 (2006) 927–935.
- [45] D. Regonini, A. Jaroenworarluck, R. Stevensa, C.R. Bowen, *Surf. Interface Anal.* 42 (2010) 139–144.
- [46] M.B. Radoičić, M. Milošević, D. Miličević, E. Suljovrujić, G. Ćirić-Marjanović, M. Radetić, Z. Šaponjić, *Surf. Coat. Technol.* 278 (2015) 38–47.
- [47] T. Rajh, A.E. Ostafin, O. Mičić, D. Tiede, M. Thurnauer, *J. Phys. Chem.* 100 (1996) 4538–4545.
- [48] M. Trchová, E.N. Konyushenko, J. Stejskal, J. Kovarova, G. Ćirić-Marjanović, *Polym. Degrad. Stab.* 94 (2009) 929–938.
- [49] J. Robertson, *Mater. Sci. Eng. R* 37 (2002) 129–281.
- [50] O. Akhavan, *ACS Nano* 4 (2010) 4174–4180.
- [51] J. Filik, *Spectrosc. Eur.* 17 (2005) 10–17.
- [52] A. Janošević, I. Pašti, N. Gavrilov, S. Mentus, J. Krstić, M. Mitrić, J. Travas-Sejdic, G. Ćirić-Marjanović, *Microporous Mesoporous Mater.* 152 (2012) 50–57.
- [53] R. Arrigo, M. Hävecker, S. Wrabetz, R. Blume, M. Lerch, J. McGregor, *J. Am. Chem. Soc.* 132 (2010) 9616–9630.
- [54] A.J. Ležaić, D. Bajuk-Bogdanović, M. Radoičić, V. Mirsky, G. Ćirić-Marjanović, *Synth. Met.* 214 (2016) 35–44.
- [55] R. Enriquez, P. Pichat, *Langmuir* 17 (2001) 6132–6137.
- [56] J.W. Peterson, B. Gu, M. Seymour, *Sci. Total Environ.* 532 (2015) 398–403.
- [57] N.P. Sokolova, A.M. Gorbunov, R.A. Bulgakova, I.A. Polunina, *Prot. Met. Phys. Chem.* 45 (2009) 685–692.
- [58] Y. Li, Y. Yu, L. Wu, J. Zhi, *Appl. Surf. Sci.* 273 (2013) 135–143.
- [59] D. Hanaor, C. Sorrell, *J. Mater. Sci.* 46 (2011) 855–874.
- [60] T. Mazza, E. Barborini, P. Piseri, P. Milani, D. Cattaneo, A. Li Bassi, C.E. Bottani, C. Ducati, *Phys. Rev. B* 75 (2007) 5, 045416.
- [61] A.S. Attar, Z. Hassani, *J. Mater. Sci. Technol.* 31 (2015) 828–833.
- [62] C.G. Silva, J.L. Faria, *App. Catal. B: Environ.* 101 (2010) 81–89.
- [63] Y. Ou, J.D. Lin, S.M. Fang, D.W. Liao, *Chem. Phys. Lett.* 429 (2006) 199–203.
- [64] K. Dai, T.Y. Peng, D.N. Ke, B.Q. Wei, *Nanotechnology* 20 (2009) 1–6.
- [65] T. Fotiou, T.M. Triantis, T. Kaloudis, L.M. Pastrana-Martínez, V. Likodimos, P. Falaras, A.M.T. Silva, A. Hiskia, *Ind. Eng. Chem. Res.* 52 (2013) 13991–14000.
- [66] B. Gao, G.Z. Chen, G. Li Puma, *Appl. Catal. B: Environ.* 89 (2009) 503–509.
- [67] M.J. Sampaio, R.R. Bacsá, A. Benyounes, R. Axet, P. Serp, C.G. Silva, A.M.T. Silva, J.L. Faria, *J. Catal.* 331 (2015) 172–180.
- [68] D. Qu, M. Zheng, P. Du, Y. Zhou, L. Zhang, D. Li, H. Tan, Z. Zhao, Z. Xie, Z. Sun, *Nanoscale* 5 (2013) 12272–12277.
- [69] Y. Li, Y. Zhao, H. Cheng, Y. Hu, G. Shi, L. Dai, L. Qu, *J. Am. Chem. Soc.* 134 (2012) 15–18.
- [70] M. Liu, L. Piao, L. Zhao, S. Ju, Z. Yan, T. He, C. Zhou, W. Wang, *Chem. Commun.* 46 (2010) 1664–1666.
- [71] H. Charles, P.D. Anthony, A.E. Ian, *J. Colloid Interf. Sci.* 4 (1974) 766–778.
- [72] D. Hurum, A. Agrios, K. Gray, T. Rajh, M. Thurnauer, *J. Phys. Chem. B* 107 (2003) 4545–4549.
- [73] Z. Mou, Y. Wu, J. Sun, P. Yang, Y. Du, C. Lu, *ACS Appl. Mater. Interfaces* 6 (2014) 13798–13806.
- [74] P. Wang, Z. Wang, L. Jia, Z. Xiao, *Phys. Chem. Chem. Phys.* 11 (2009) 2730–2740.
- [75] L. Yingliang, S. Wang, S. Xu, S. Cao, *Mater. Res. Bull.* 65 (2015) 27–35.
- [76] Y. Xu, Y. Mo, J. Tian, P. Wang, H. Yu, J. Yu, *App. Catal. B: Environ.* 181 (2016) 810–817.
- [77] R. Su, R. Bechstein, L. So, R. Vang, M. Sillassen, B. Esbjornsson, A. Palmqvist, F. Besenbacher, *J. Phys. Chem. C* 115 (2011) 24287–24292.
- [78] Z. Xiong, H. Wu, L. Zhang, Y. Gu, X.S. Zhao, *J. Mater. Chem. A* 2 (2014) 9291–9297.